Time-dependent Aero-elastic Adjoint-based Aerodynamic Shape Optimization of Helicopter Rotors in Forward Flight

Asitav Mishra * Dimitri Mavriplis †

Jay Sitaraman ‡

Department of Mechanical Engineering,University of Wyoming, Laramie, WY 82071-3295.

A formulation for sensitivity analysis of fully coupled time-dependent aeroelastic problems is given in this paper. This work is an extension of a previously derived formulation to incorporate periodically varying rotor pitch angle as design parameters to perform rotor shape optimization in forward flight conditions. Both forward sensitivity and adjoint sensitivity formulations are derived that correspond to analogues of the non-linear aeroelastic analysis problem. Both sensitivity analysis formulations make use of the same iterative disciplinary solution techniques used for analysis, and make use of an analogous coupling strategy. The fully coupled aeroelastic analysis formulation is first verified to effectively perform performance predictions of a four bladed HART2 rotor in forward flight started impulsively from rest. Upon successful verification of the fully coupled adjoint formulation, it is used to perform trim and aerodynamic shape design optimization for helicopter rotors in forward flight conditions.

I. Introduction

Adjoint equations, popular for aerodynamic shape optimization problems using computational fluid dynamics (CFD), [1–9] are a very powerful tool in the sense that they allow the computation of sensitivity derivatives of an objective function to a set of given inputs at a cost which is essentially independent of the number of inputs. While the use of adjoint equations is now fairly well established in steady-state shape optimization, only recently have inroads been made into extending them to unsteady flow problems. Preliminary demonstration of the method's feasibility in three-dimensional problems was done by Mavriplis.[10] Full implementation in a general sense and application to large scale problems involving helicopter rotors was then carried out by Nielsen et. al. in the NASA FUN3D code[12,13] and by Mani et. al.[14]

Since engineering optimization is an inherently multidisciplinary endeavor, the next logical step involves extending adjoint methods to multidisciplinary simulations and using the obtained sensitivities for driving multidisciplinary optimizations. In the context of fixed and especially rotary wing aircraft, aeroelastic coupling effects can be very important and must be considered in the context of a successful optimization strategy. The coupling of computational fluid dynamics (CFD) and computational structural dynamics (CSD) and the use of sensitivity analysis on such a system has been addressed in the past primarily from a steady-state standpoint.[15,16] Until now, relatively little work has been done addressing unsteady aeroelastic optimization problems, mainly due to complexities in the linearization of coupled time-dependent systems. In previous work,[17,18] a time-dependent three-dimensional aeroelastic adjoint formulation for helicopter rotor optimization problems was derived. This work built upon a previously demonstrated time-dependent aerodynamic optimization capability that was applied to helicopter rotors in reference[14] through the addition of a Hodges-Dowell type beam finite-element model to simulate the rotor structure, and the development of the fully coupled discrete adjoint of the resulting aeroelastic system. This work demonstrated the effectiveness of using this approach for performing aeroelastic optimization of a representative rotorcraft configuration in hover conditions.

The aim of current work is to extend the formulation to include time-dependent rotor pitch inputs to accommodate forward flight analysis. For shape optimization of rotors in forward flight, pitch inputs not only can feature as design parameters, but also can allow for strong rotor trim constraints by making use of force and moment sensitivities with respect to pitch inputs.

*Postdoctoral Research Associate; amishra3@uwyo.edu

†Professor; mavripl@uwyo.edu

‡Associate Professor; jsitaram@uwyo.edu

II. Aerodynamic Analysis and Sensitivity Formulation

II.A. Flow Solver Analysis Formulation

The base flow solver used in this work is the NSU3D unstructured mesh Reynolds-averaged Navier-Stokes solver. NSU3D has been widely validated for steady-state and time-dependent flows and contains a discrete tangent and adjoint sensitivity capability which has been demonstrated previously for optimization of steady-state and time-dependent flow problems. As such, only a concise description of these formulations will be given in this paper, with additional details available in previous references.[14,17,19,20] The flow solver is based on the conservative form of the Navier-Stokes equations which may be written as:

$$\frac{\partial \mathbf{U}(\mathbf{x},t)}{\partial t} + \nabla \cdot \mathbf{F}(\mathbf{U}) = 0 \tag{1}$$

For moving mesh problems these are written in arbitrary Lagrangian-Eulerian (ALE) form as:

$$\frac{\partial V\mathbf{U}}{\partial t} + \int_{dB(t)} [\mathbf{F}(\mathbf{U}) - \dot{\mathbf{x}}\mathbf{U}] \cdot \mathbf{n} dB = 0 \tag{2}$$

Here V refers to the area of the control volume, $\dot{\mathbf{x}}$ is the vector of mesh face or edge velocities, and $\mathbf{n}$ is the unit normal of the face or edge. The state vector $\mathbf{U}$ consists of the conserved variables and the Cartesian flux vector $\mathbf{F} = (\mathbf{F}_x, \mathbf{F}_y, \mathbf{F}_z)$ contains both inviscid and viscous fluxes. The equations are closed with the perfect gas equation of state and the Spalart-Allmaras turbulent eddy viscosity model[21] for all cases presented in this work.

The solver uses a vertex-centered median dual control volume formulation that is second-order accurate, where the inviscid flux integral S around a closed control volume is discretized as:

$$S = \int_{dB(t)} [\mathbf{F}(\mathbf{U}) - \dot{\mathbf{x}}\mathbf{U}] \cdot \mathbf{n} dB = \sum_{i=1}^{n_{edge}} \mathbf{F}_{e_i}^{\perp}(V_{e_i}, \mathbf{U}, \mathbf{n}_{ei}) B_{e_i} \tag{3}$$

where B_e is the face area, V_e is the normal face velocity, $\mathbf{n}_e$ is the unit normal of the face, and $F_e^{\perp}$ is the normal flux across the face. The time derivative term is discretized using a second-order accurate backward-difference formula (BDF2) scheme. Denoting the spatially discretized terms at time level n by the operator $S^n(\mathbf{U}^n)$, the resulting system of non-linear equations to be solved for the analysis problem at each time step can be written as:

$$\mathbf{R}^n = \frac{\frac{3}{2}V^n\mathbf{U}^n - 2V^{n-1}\mathbf{U}^{n-1} - \frac{1}{2}V^{n-2}\mathbf{U}^{n-2}}{\Delta t} + S^n(\mathbf{U}^n) = 0 \tag{4}$$

which in simplified form exhibiting the functional dependencies on $\mathbf{U}$ and $\mathbf{x}$ at different time levels is given as:

$$\mathbf{R}^n(\mathbf{U}^n, \mathbf{U}^{n-1}, \mathbf{U}^{n-2}, \mathbf{x}^n, \mathbf{x}^{n-1}, \mathbf{x}^{n-2}) = 0 \tag{5}$$

At each time step n, the implicit residual is linearized with respect to the unknown solution vector $\mathbf{U}^n$ and solved for using Newton's method as:

$$\begin{aligned} \left[\frac{\partial \mathbf{R}^k}{\partial \mathbf{U}^k}\right] \delta\mathbf{U}^k &= -\mathbf{R}^k \\ \mathbf{U}^{k+1} &= \mathbf{U}^k + \delta\mathbf{U}^k \\ \delta\mathbf{U}^k \rightarrow 0, \mathbf{U}^n &= \mathbf{U}^k \end{aligned} \tag{6}$$

The Jacobian matrix is inverted iteratively using a line-implicit agglomeration multigrid scheme that can also be used as a preconditioner for a GMRES Krylov solver.[22]

Although the above equation denotes the solution at a single time level n, for the remainder of this paper we will use the generalized notation:

$$\mathbf{R}(\mathbf{U}, \mathbf{x}) = 0 \tag{7}$$

where the vector $\mathbf{U}$ denotes the flow values at all time steps, and where each (block) row in this equation corresponds to the solution at a particular time step as given in equation (5). Equation (7) denotes the simultaneous solution of all time steps and is solved in practice by Newton's method using forward block substitution (i.e. forward integration in time) since each new time step depends on the previous two time levels.

II.B. Mesh deformation capability

In order to deform the mesh for time-dependent problems a spring analogy and a linear elastic analogy mesh deformation approach have been implemented. The linear elasticity approach has proven to be much more robust and is used exclusively in this work. In this approach, the mesh is modeled as a linear elastic solid with a variable modulus of elasticity that can be prescribed either as inversely proportional to cell volume or to the distance of each cell from the nearest wall.[23,24] The resulting equations are discretized and solved on the mesh in its original undeformed configuration in response to surface displacements using a line-implicit multigrid algorithm analogous to that used for the flow equations. The governing equations for mesh deformation can be written symbolically as:

$$\mathbf{G}(\mathbf{x},\mathbf{D}) = \mathbf{0} \tag{8}$$

where $\mathbf{x}$ denotes the interior mesh coordinates and $\mathbf{D}$ denotes shape parameters that define the surface geometry.

III. Aerodynamic Sensitivity Analysis Formulation

The basic sensitivity analysis implementation follows the strategy developed in references.[10,19] Consider an arbitrary objective function L that is evaluated using the unsteady flow solution set $\mathbf{U}$ and unsteady mesh solution set $\mathbf{x}$ expressed as:

$$L = L(\mathbf{U},\mathbf{x}) \tag{9}$$

Assuming that the state variables (i.e.$\mathbf{U},\mathbf{x}$) are dependent on some input design parameters $\mathbf{D}$, the total sensitivity of the objective function L to the set of design inputs can be expressed as the inner product between the vector of state sensitivities to design inputs and the vector of objective sensitivities to the state variables as:

$$\frac{dL}{d\mathbf{D}} = \begin{bmatrix} \dfrac{\partial L}{\partial \mathbf{x}} & \dfrac{\partial L}{\partial \mathbf{U}} \end{bmatrix} \begin{bmatrix} \dfrac{\partial \mathbf{x}}{\partial \mathbf{D}} \\ \dfrac{\partial \mathbf{U}}{\partial \mathbf{D}} \end{bmatrix} \tag{10}$$

The non-linear flow residual operator and the linear elasticity mesh residual operator as described earlier provide the constraints which can be expressed in general form over the whole space and time domains as:

$$\mathbf{G}(\mathbf{x},\mathbf{D}) = 0 \tag{11}$$

$$\mathbf{R}(\mathbf{U},\mathbf{x}) = 0 \tag{12}$$

which when linearized with respect to the design inputs yields:

$$\begin{bmatrix} \dfrac{\partial \mathbf{G}}{\partial \mathbf{x}} & 0 \\ \dfrac{\partial \mathbf{R}}{\partial \mathbf{x}} & \dfrac{\partial \mathbf{R}}{\partial \mathbf{U}} \end{bmatrix} \begin{bmatrix} \dfrac{\partial \mathbf{x}}{\partial \mathbf{D}} \\ \dfrac{\partial \mathbf{U}}{\partial \mathbf{D}} \end{bmatrix} = \begin{bmatrix} -\dfrac{\partial \mathbf{G}}{\partial \mathbf{D}} \\ 0 \end{bmatrix} \tag{13}$$

These constitute the forward sensitivity or tangent sensitivity equations. The mesh and flow sensitivity vectors can then be substituted into equation (10) to obtain the complete sensitivity of the objective with respect to the design variable $\mathbf{D}$.

The forward sensitivity approach requires a new solution of equation (13) for each design parameter $\mathbf{D}$. On the other hand, the adjoint approach can obtain the sensitivities for any number of design inputs $\mathbf{D}$ at a cost which is independent of the number of design variables. The adjoint problem can be obtained by pre-multiplying equation (13) by the inverse of the large coupled matrix and substituting the resulting expression for the sensitivities into equation (10) and defining adjoint variables as the solution of the system:

$$\begin{bmatrix} \dfrac{\partial \mathbf{G}}{\partial \mathbf{x}}^T & \dfrac{\partial \mathbf{R}}{\partial \mathbf{x}}^T \\ 0 & \dfrac{\partial \mathbf{R}}{\partial \mathbf{U}}^T \end{bmatrix} \begin{bmatrix} \Lambda_{\mathbf{x}} \\ \Lambda_{\mathbf{U}} \end{bmatrix} = \begin{bmatrix} \dfrac{\partial L}{\partial \mathbf{x}}^T \\ \dfrac{\partial L}{\partial \mathbf{U}}^T \end{bmatrix} \tag{14}$$

where $\Lambda_{\mathbf{U}}$ and $\Lambda_{\mathbf{x}}$ are the flow and mesh adjoint variables respectively. The final objective sensitivities can be obtained as:

$$\frac{dL}{d\mathbf{D}}^T = \begin{bmatrix} \frac{\partial \mathbf{G}}{\partial \mathbf{D}}^T & 0 \end{bmatrix} \begin{bmatrix} \Lambda_{\mathbf{x}} \\ \Lambda_{\mathbf{u}} \end{bmatrix} \tag{15}$$

Recalling that equation (14) applies over the entire time domain, the back-substitution procedure leads to a reverse integration in time, beginning with the last physical time step and proceeding to the initial time step. A more detailed description of the complete formulation is presented in,[25] where the procedure has been used to perform aerodynamic shape optimization for a rigid rotor.

IV. Beam model: Analysis and Adjoint Optimization

A non-linear bend-twist beam model is a suitable and widely utilized structural model for slender fixed and rotary wing aircraft structures within the context of an aeroelastic problem. A bend-twist beam model, described below, has previously been developed and coupled to the NSU3D unstructured mesh Reynolds-averaged Navier-Stokes solver.[24,26]

IV.A. Beam Analysis Formulation

The non-linear governing equations of a slender beam are discretized using the Finite-element method (FEM) in space. Figure 1 shows a typical beam with 15 degrees of freedom for each element to accommodate bend wise, lag wise, axial and torsional displacements. The second order equation of motion for the beam can be expressed as:

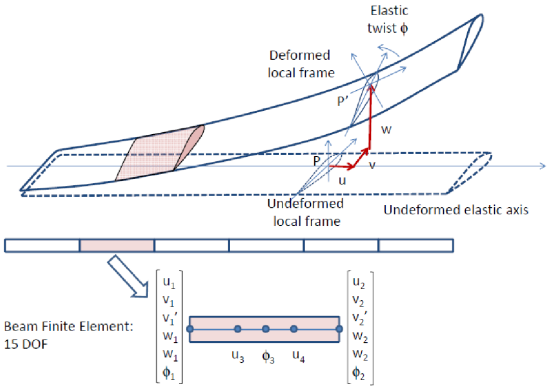

Figure 1. 15 degrees of freedom beam element with flap, lag, torsional and axial degrees of freedom.

$$[M]\ddot{\mathbf{q}} + [C]\dot{\mathbf{q}} + [K] = F \tag{16}$$

where $[M]$, $[C]$ and $[K]$ are mass, damping and stiffness matrices of the system of equations representing the beam. Vector $F = F(t)$ is the forcing vector. Vector $\mathbf{q}$ represents the displacements along all degrees of freedom. This set of equations can be reduced to a first order system and solved using a second order backward difference formula (BDF2) time integration with standard Newton-type linearization and sub-iterations to efficiently invert the implicit system:

$$[I]\dot{\mathbf{Q}} + [A]\mathbf{Q} = \mathbf{F} \tag{17}$$

where $[I]$ is the identity matrix, $\mathbf{Q} = [\mathbf{q}, \dot{\mathbf{q}}]^T$, $\mathbf{F} = [0,\ [M]^{-1}F]^T$ and $[A] = \begin{bmatrix} 0 & -[I] \\ [M]^{-1}[K] & [M]^{-1}[C] \end{bmatrix}$. The residual of the structural equations can be defined as: $\mathbf{J} = [I]\ \dot{\mathbf{Q}} + [A]\ \mathbf{Q} - \mathbf{F} = 0$, and can be expressed in a simplified form as:

$$\mathbf{J}(\mathbf{Q}, \mathbf{F}) = \mathbf{0} \tag{18}$$

The beam model has been validated[27] for the standard Hart-2 rotor case[28] by comparing its natural frequency predictions with the predictions from other reliable CSD models.[29]

IV.B. Forward Sensitivity Formulation of Beam Model

The beam tangent (forward sensitivity) linearization is similar to the analysis problem. For a given function, L, its sensitivity with respect to a blade design parameter, $\mathbf{D}$ can be written as: $\frac{dL}{\mathbf{dD}} = \frac{\partial L}{\partial \mathbf{D}} + \frac{\partial L}{\partial \mathbf{Q}}\frac{\partial \mathbf{Q}}{\partial \mathbf{D}}$. This requires solving for sensitivity of the beam state (Q), which can be obtained by differentiating Eqn. (18) with respect to the design variable $\mathbf{D}$ and rearranging as:

$$\left[\frac{\partial \mathbf{J}}{\partial \mathbf{Q}}\right]\frac{\partial \mathbf{Q}}{\partial \mathbf{D}} = -\frac{\partial \mathbf{J}}{\partial \mathbf{F}}\frac{\partial \mathbf{F}}{\partial \mathbf{D}} - \frac{\partial \mathbf{J}}{\partial \mathbf{D}} \tag{19}$$

The last term on the right hand side is non zero for structural design parameters such as beam element stiffnesses, in which case the applied force does not change with the design parameter, making the first term on the right hand size zero. In the coupled aeroelastic case, using aerodynamic shape parameters that primarily affect the airloads on the structure, the first term on the right-hand size is non-zero while the second term vanishes. Solving for $\frac{\partial \mathbf{Q}}{\partial \mathbf{D}}$ in Eqn. (19), the forward sensitivity of the objective function $\frac{dL}{d\mathbf{D}}$ can be obtained.

IV.C. Adjoint Formulation of Beam Model

The adjoint formulation of the beam model can be derived by approaching the tangent formulation in the reverse (transpose) direction. Taking the transpose of the objective functional sensitivity yields:

$$\frac{dL}{\mathbf{dD}}^T = \frac{\partial L}{\partial \mathbf{D}}^T + \frac{\partial \mathbf{Q}}{\partial \mathbf{D}}^T\frac{\partial L}{\partial \mathbf{Q}}^T \tag{20}$$

This requires solving for the transpose sensitivity of the beam state (Q). The solution of $\frac{\partial \mathbf{Q}}{\partial \mathbf{D}}^T$ can be derived by transposing Eqn. (19) and substituting into Eqn. (20). This requires solving for an adjoint vector $\Lambda_\mathbf{Q}$ defined as:

$$\left[\frac{\partial \mathbf{J}}{\partial \mathbf{Q}}\right]^T \Lambda_\mathbf{Q} = \frac{\partial \mathbf{L}}{\partial \mathbf{Q}}^\mathbf{T} \tag{21}$$

The above forms the adjoint formulation of the beam model. It is observed here again that the left hand side Jacobian term of the adjoint step is just the transpose of the Jacobian in the forward linearization. In previous works,[17,27] forward and adjoint formulations of the beam solver have been implemented and verified for both structural design parameters, and force-based design parameters (as required for the coupled aeroelasticity problem). The beam adjoint formulation was used to perform time-dependent structural optimizations using the large-scale bound constraint optimization tool (L-BFGS-B)[30] as a precursor to their use in fully coupled aero-structural optimization problems.

V. Fully Coupled Fluid-Structure Analysis Formulation

V.A. Fluid-structure interface (FSI)

In addition to the solution of the aerodynamic problem and the structural dynamics problem, the solution of the fully coupled time-dependent aeroelastic problem requires the exchange of aerodynamic loads from the CFD solver to the beam structure, which in turn returns surface displacements to the fluid flow solver. The governing equations for the FSI can be written in residual form as:

$$\mathbf{S}(\mathbf{F_b}, \mathbf{Q}, \mathbf{F}(\mathbf{x}, \mathbf{u})) = \mathbf{F_b} - [T(\mathbf{Q})]\mathbf{F}(\mathbf{x}, \mathbf{u}) = 0 \tag{22}$$

$$\mathbf{S}'(\mathbf{x_s}, \mathbf{Q}) = \mathbf{x_s} - [T(\mathbf{Q})]^T\mathbf{Q} = 0 \tag{23}$$

respectively for the forces transfered to the structural solver and displacements returned to the flow solver. In these equations, $[T]$ represents the transfer matrix which projects point-wise CFD surface forces $\mathbf{F}(\mathbf{x}, \mathbf{u})$ onto the individual beam elements resulting in the beam forces $\mathbf{F_b}$. The transpose of this matrix is used to obtain the CFD surface displacements $\mathbf{x_s}$ from the beam degrees of freedom $\mathbf{Q}$. Also note that $[T]$ is a function of $\mathbf{Q}$ since the transfer patterns change with the beam deflection.

V.B. General solution procedure

The aeroelastic problem consists of multiple coupled sets of equations namely, the mesh deformation equations, the flow equations (CFD), the beam model-based structural equations, and the fluid-structure interface transfer equations.

The system of equations to be solved at each time step can be written as:

$$\mathbf{G}(\mathbf{x}, \mathbf{x_s}(\mathbf{Q})) = \mathbf{0} \tag{24}$$

$$\mathbf{R}(\mathbf{u}, \mathbf{x}) = \mathbf{0} \tag{25}$$

$$\mathbf{S}(\mathbf{F_B}, \mathbf{Q}, \mathbf{F}(\mathbf{x}, \mathbf{u})) = \mathbf{0} \tag{26}$$

$$\mathbf{J}(\mathbf{Q}, \mathbf{F_B}) = \mathbf{0} \tag{27}$$

$$\mathbf{S'}(\mathbf{x_s}, \mathbf{Q}) = \mathbf{0} \tag{28}$$

where $\mathbf{S}$ and $\mathbf{S'}$ represent the residuals of the FSI equations, and J represents the residual of the structural analysis problem. Note that the mesh motion residual now depends also on any surface deflections $\mathbf{x_s}$ introduced by the structural model. Within each physical time step, solution of the fully coupled fluid structure problem consists of performing multiple coupling iterations on each discipline using the latest available values from the other disciplines.

At the first coupling iteration, $\mathbf{x_s^c} = \mathbf{0}$ (superscript $\mathbf{c}$ denotes the coupling iteration index) and solution of the mesh deformation equation is trivial, although non zero values of $\mathbf{x_s}$ are produced at subsequent coupling iterations as the beam deflects in response to the aero loads. From a disciplinary point of view, the aerodynamic solver produces updated values of $\mathbf{u}$ and $\mathbf{x}$, which are used to compute $\mathbf{F}(\mathbf{x}, \mathbf{u})$ pointwise surface forces. These surface forces are input to the FSI/structural model which returns surface displacements $\mathbf{x_s}$. These new surface displacements are then fed back into the mesh deformation equations and the entire procedure is repeated until convergence is obtained for the full coupled aero-structural problem at the given time step.

VI. Sensitivity Analysis for Coupled Aeroelastic Problem

In the formulation of the sensitivity analysis for the coupled aeroelastic problem, it is desirable to mimic as closely as possible the solution strategies and data structures employed for the analysis problem. Thus, analogous disciplinary solvers can be reused for each disciplinary sensitivity problem, and the analysis coupling strategy can be extended to the sensitivity analysis formulation. Furthermore, the data transfered between disciplinary solvers should consist of vectors of the same dimension for the analysis, tangent and adjoint formulations. Starting with the forward sensitivity problem, the sensitivity of an objective L can be written as:

$$\frac{dL}{d\mathbf{D}} = \begin{bmatrix} \frac{\partial L}{\partial \mathbf{x}} & \frac{\partial L}{\partial \mathbf{u}} \end{bmatrix} \begin{bmatrix} \frac{\partial \mathbf{x}}{\partial \mathbf{D}} \\ \frac{\partial \mathbf{u}}{\partial \mathbf{D}} \end{bmatrix} \tag{29}$$

where the individual disciplinary sensitivities are given as the solution of the coupled system:

$$\begin{bmatrix} \frac{\partial \mathbf{G}}{\partial \mathbf{x}} & 0 & 0 & 0 & 0 & \frac{\partial \mathbf{G}}{\partial \mathbf{x_s}} \\ \frac{\partial \mathbf{R}}{\partial \mathbf{x}} & \frac{\partial \mathbf{R}}{\partial \mathbf{u}} & 0 & 0 & 0 & 0 \\ -\frac{\partial \mathbf{F}}{\partial \mathbf{x}} & -\frac{\partial \mathbf{F}}{\partial \mathbf{u}} & I & 0 & 0 & 0 \\ 0 & 0 & \frac{\partial \mathbf{S}}{\partial \mathbf{F}} & \frac{\partial \mathbf{S}}{\partial \mathbf{F_b}} & \frac{\partial \mathbf{S}}{\partial \mathbf{Q}} & 0 \\ 0 & 0 & 0 & \frac{\partial \mathbf{J}}{\partial \mathbf{F_b}} & \frac{\partial \mathbf{J}}{\partial \mathbf{Q}} & 0 \\ 0 & 0 & 0 & 0 & \frac{\partial \mathbf{S'}}{\partial \mathbf{Q}} & \frac{\partial \mathbf{S'}}{\partial \mathbf{x_s}} \end{bmatrix} \begin{bmatrix} \frac{\partial \mathbf{x}}{\partial \mathbf{D}} \\ \frac{\partial \mathbf{u}}{\partial \mathbf{D}} \\ \frac{\partial \mathbf{F}}{\partial \mathbf{D}} \\ \frac{\partial \mathbf{F_b}}{\partial \mathbf{D}} \\ \frac{\partial \mathbf{Q}}{\partial \mathbf{D}} \\ \frac{\partial \mathbf{x_s}}{\partial \mathbf{D}} \end{bmatrix} = \begin{bmatrix} -\frac{\partial \mathbf{G}}{\partial \mathbf{D}} \\ 0 \\ 0 \\ 0 \\ 0 \\ 0 \end{bmatrix}$$

The first and second equations correspond to equations for the mesh and flow variable sensitivities, as previously described for the aerodynamic solver, and the third equation corresponds to the construction of the surface force

sensitivities given these two previous sensitivities. The fourth equation denotes the sensitivity of the FSI transfer from the fluid to the structural solver, while the fifth equation corresponds to the sensitivity of the structural solver. Finally, the last equation corresponds to the sensitivity of the FSI transfer from the structural solver back to the flow solver. As can be seen, each disciplinary solution procedure requires the inversion of the same Jacobian matrix as the corresponding analysis problem, which is done using the same iterative solver. Furthermore, the fluid-structure coupling requires the transfer of the force sensitivities $\frac{\partial \mathbf{F}}{\partial \mathbf{D}}$ from the flow to the structural solver, and the surface mesh sensitivities $\frac{\partial \mathbf{x_s}}{\partial \mathbf{D}}$ from the structural solver back to the fluid solver, which are of the same dimension as the force and surface displacements transfered in the analysis problem, respectively.

The corresponding adjoint problem can be obtained by pre-multiplying equation (30) by the inverse of the large coupling matrix and substituting this into equation (29), transposing the entire system, and defining adjoint variables as solutions to the following coupled system:

$$\begin{bmatrix} \frac{\partial \mathbf{G}}{\partial \mathbf{x}}^T & \frac{\partial \mathbf{R}}{\partial \mathbf{x}}^T & -\frac{\partial \mathbf{F}}{\partial \mathbf{x}}^T & 0 & 0 & 0 \\ 0 & \frac{\partial \mathbf{R}}{\partial \mathbf{u}}^T & -\frac{\partial \mathbf{F}}{\partial \mathbf{u}}^T & 0 & 0 & 0 \\ 0 & 0 & I & \frac{\partial \mathbf{S}}{\partial \mathbf{F}}^T & 0 & 0 \\ 0 & 0 & 0 & \frac{\partial \mathbf{S}}{\partial \mathbf{F_b}}^T & \frac{\partial \mathbf{J}}{\partial \mathbf{F_b}}^T & 0 \\ 0 & 0 & 0 & \frac{\partial \mathbf{S}}{\partial \mathbf{Q}}^T & \frac{\partial \mathbf{J}}{\partial \mathbf{Q}}^T & \frac{\partial \mathbf{S}'}{\partial \mathbf{Q}}^T \\ \frac{\partial \mathbf{G}}{\partial \mathbf{x_s}}^T & 0 & 0 & 0 & 0 & \frac{\partial \mathbf{S}'}{\partial \mathbf{x_s}}^T \end{bmatrix} \begin{bmatrix} \Lambda_{\mathbf{x}} \\ \Lambda_{\mathbf{u}} \\ \Lambda_{\mathbf{F}} \\ \Lambda_{\mathbf{F_b}} \\ \Lambda_{\mathbf{Q}} \\ \Lambda_{\mathbf{x_s}} \end{bmatrix} = \begin{bmatrix} \frac{\partial \mathbf{L}}{\partial \mathbf{x}}^T \\ \frac{\partial \mathbf{L}}{\partial \mathbf{u}}^T \\ 0 \\ 0 \\ 0 \\ 0 \end{bmatrix} \tag{30}$$

Once again, the solution of the various disciplinary adjoint equations requires the inversion of the corresponding disciplinary Jacobians (transposed in this case) which can be accomplished using the same iterative solvers as for the analysis and forward sensitivity problems. Additionally, the input to the structural adjoint problem consists of the variable $\Lambda_{\mathbf{x_s}}$, which is the same dimension as the surface displacements output from the structural analysis solver, while the output of the structural adjoint solver consists of the variable $\Lambda_{\mathbf{F}}$ which is of the same dimension as the force inputs to the structural solver in the analysis problem. Detailed description of the solution procedure for the coupled adjoint formulation can be found in the author's previous works.[17,18]

VI.A. Pitch Formulations for Forward Flight: Analysis and Sensitivity

As mentioned earlier, the goal of this work is to incorporate rotor pitch angle ($\theta(\psi)$, ψ being rotor azimuth) as control inputs. Pitch angle can be represented by a combination of mean pitch angle (θ_0) and several harmonic components of pitch angles (e.g. θ_{c_i} and θ_{s_i} for i'th harmonic): $\theta = \theta_0 + \theta_{c_i} cos(i\psi) + \theta_{s_i} sin(i\psi)$, for harmonics of $i = [1, 2, \cdots]$. This introduces a new set of design parameters, i.e. $\mathbf{D} = [\theta, \theta_{\mathbf{c_i}}, \theta_{\mathbf{s_i}}]$, and thus provides more optimization control. This section describes the formulation for adjoint sensitivities of a time dependent objective function with respect to the pitch angle design parameters for a rigid rotor in forward flight. The formulation can be easily extended to a flexible rotor blade.

To incorporate rotor pitch actuation two additional equations need to be considered: i) a pitch actuation equation, represented by $\mathbf{S}^{\theta}(\mathbf{x}_{s\theta}, \mathbf{x}) = \mathbf{x}_{s\theta} - [\mathbf{T}^{\theta}(\theta(\mathbf{D}))]\mathbf{x} = \mathbf{0}$, and ii) a mesh motion equation to propagate surface displacements due to pitch to the interior mesh: $\mathbf{G}'(\mathbf{x}_{\theta}, \mathbf{x}_{s\theta}) = \mathbf{0}$. Here $\mathbf{x}_{s\theta}$ denotes the surface mesh coordinates after pitch and $\mathbf{x}_{\theta}$ denotes the interior mesh coordinates after mesh motion due to pitch. Introducing a constraint equation for mesh rotation: $\mathbf{S}^{\psi}(\mathbf{x_p}, \mathbf{x}_{\theta}) = \mathbf{x_p} - [\mathbf{T}^{\psi}]\mathbf{x}_{\theta} = \mathbf{0}$ ($\mathbf{x_p}$ denotes the interior mesh after rotation) and using the mesh deformation equation to accommodate blade sensitivity, the analysis formulation with pitch and rotation (without aero-elastic coupling) can

be represented as:

$$\mathbf{G}(\mathbf{x},\mathbf{D}) = \mathbf{0} \tag{31}$$
$$\mathbf{S}^{\theta}(\mathbf{x}_{s\theta},\mathbf{x},\mathbf{D}) = \mathbf{0} \tag{32}$$
$$\mathbf{G}'(\mathbf{x}_{\theta},\mathbf{x}_{s\theta}) = \mathbf{0} \tag{33}$$
$$\mathbf{S}^{\Psi}(\mathbf{x}_{\mathbf{p}},\mathbf{x}_{\theta}) = \mathbf{0} \tag{34}$$
$$\mathbf{R}(\mathbf{x}_{\mathbf{p}},\mathbf{u}) = \mathbf{0} \tag{35}$$

Here $[\mathbf{T}^{\theta}]$ and $[\mathbf{T}^{\Psi}]$ are matrix representations for pitch actuation and rotation, respectively. Although the solid body mesh rotation constraint is present in all cases, it has been omitted for simplicity in the previous formulation, but is included explicitly in this case to differentiate between the two types of prescribed motion (namely blade pitch and rotation). The forward sensitivity formulation of the pitching actuation mimics the analysis formulation described above and is obtained by linearizing these equations with respect to the design variables, which yields:

$$\begin{bmatrix} \frac{\partial \mathbf{G}}{\partial \mathbf{x}} & 0 & 0 & 0 & 0 \\ \frac{\partial \mathbf{S}^{\theta}}{\partial \mathbf{x}} & \frac{\partial \mathbf{S}^{\theta}}{\partial \mathbf{x}_{s\theta}} & 0 & 0 & 0 \\ 0 & \frac{\partial \mathbf{G}'}{\partial \mathbf{x}_{s\theta}} & \frac{\partial \mathbf{G}'}{\partial \mathbf{x}_{\theta}} & 0 & 0 \\ 0 & 0 & \frac{\partial \mathbf{S}^{\Psi}}{\partial \mathbf{x}} & \frac{\partial \mathbf{S}^{\Psi}}{\partial \mathbf{x}_{\mathbf{p}}} & 0 \\ 0 & 0 & 0 & \frac{\partial \mathbf{R}}{\partial \mathbf{x}_{\mathbf{p}}} & \frac{\partial \mathbf{R}}{\partial \mathbf{u}} \end{bmatrix} \begin{bmatrix} \frac{\partial \mathbf{x}}{\partial \mathbf{D}} \\ \frac{\partial \mathbf{x}_{s\theta}}{\partial \mathbf{D}} \\ \frac{\partial \mathbf{x}_{\theta}}{\partial \mathbf{D}} \\ \frac{\partial \mathbf{x}_{\mathbf{p}}}{\partial \mathbf{D}} \\ \frac{\partial \mathbf{u}}{\partial \mathbf{D}} \end{bmatrix} = \begin{bmatrix} -\frac{\partial \mathbf{G}}{\partial \mathbf{D}} \\ -\frac{\partial \mathbf{S}^{\theta}}{\partial \mathbf{D}} \\ 0 \\ 0 \\ 0 \end{bmatrix} \tag{36}$$

From the solution of this equation, now the sensitivity of a time dependent objective function can be obtained as: $\frac{dL}{d\mathbf{D}} = \begin{bmatrix} \frac{\partial L}{\partial \mathbf{x}} & \frac{\partial L}{\partial \mathbf{x}_{s\theta}} & \frac{\partial L}{\partial \mathbf{u}} \end{bmatrix} \begin{bmatrix} \frac{\partial \mathbf{x}}{\partial \mathbf{D}} & \frac{\partial \mathbf{x}_{s\theta}}{\partial \mathbf{D}} & \frac{\partial \mathbf{u}}{\partial \mathbf{D}} \end{bmatrix}^T$. The corresponding adjoint sensitivity formulation can be obtained by constructing a transposed Jacobian matrix from Eqn. 36 to solve for corresponding adjoint vectors $\Lambda_{\mathbf{x}}, \Lambda_{\mathbf{x}_{s\theta}}, \Lambda_{\mathbf{x}_{\theta}}, \Lambda_{\mathbf{x}_{\mathbf{p}}}$, and $\Lambda_{\mathbf{x}_{\mathbf{u}}}$:

$$\begin{bmatrix} \frac{\partial \mathbf{G}}{\partial \mathbf{x}}^T & \frac{\partial \mathbf{S}^{\theta}}{\partial \mathbf{x}}^T & 0 & 0 & 0 \\ 0 & \frac{\partial \mathbf{S}^{\theta}}{\partial \mathbf{x}_{s\theta}}^T & \frac{\partial \mathbf{G}'}{\partial \mathbf{x}_{s\theta}}^T & 0 & 0 \\ 0 & 0 & \frac{\partial \mathbf{G}'}{\partial \mathbf{x}_{\theta}}^T & \frac{\partial \mathbf{S}^{\Psi}}{\partial \mathbf{x}_{\theta}}^T & 0 \\ 0 & 0 & 0 & \frac{\partial \mathbf{S}^{\Psi}}{\partial \mathbf{x}_{\mathbf{p}}}^T & \frac{\partial \mathbf{R}}{\partial \mathbf{x}_{\mathbf{p}}}^T \\ 0 & 0 & 0 & 0 & \frac{\partial \mathbf{R}}{\partial \mathbf{u}}^T \end{bmatrix} \begin{bmatrix} \Lambda_{\mathbf{x}} \\ \Lambda_{\mathbf{x}_{s\theta}} \\ \Lambda_{\mathbf{x}_{\theta}} \\ \Lambda_{\mathbf{x}_{\mathbf{p}}} \\ \Lambda_{\mathbf{u}} \end{bmatrix} = \begin{bmatrix} \frac{\partial L}{\partial \mathbf{x}}^T \\ \frac{\partial L}{\partial \mathbf{x}_{s\theta}}^T \\ 0 \\ 0 \\ \frac{\partial L}{\partial \mathbf{u}}^T \end{bmatrix} \tag{37}$$

The final objective sensitivities can be obtained as: $\frac{dL}{d\mathbf{D}}^T = \begin{bmatrix} -\frac{\partial \mathbf{G}}{\partial \mathbf{D}}^T & -\frac{\partial \mathbf{S}^{\theta}}{\partial \mathbf{D}}^T & 0 & 0 & 0 \end{bmatrix} \begin{bmatrix} \Lambda_{\mathbf{x}} & \Lambda_{\mathbf{x}_{s\theta}} & \Lambda_{\mathbf{x}_{\theta}} & \Lambda_{\mathbf{x}_{\mathbf{p}}} & \Lambda_{\mathbf{u}} \end{bmatrix}^T$

Here, $\Lambda_{\mathbf{x}_{s\theta}}$ refers to adjoint contribution from the pitch sensitivity formulation. For the flexible (aeroelastic) case, the above forward and adjoint sensitivity systems are augmented by the additional structural and fluid-structure interface sensitivity/adjoint equations as described previously.

VII. Verification of Coupled Aeroelastic Sensitivity

The forward and adjoint sensitivities for the coupled aeroelastic problem are verified using the complex step method. Any function $f(x)$ operating on a real variable x can be utilized to compute the derivative $f'(x)$ by redefining the input variable x and all intermediate variables used in the discrete evaluation of $f(x)$ as complex variables. For a complex input, the function when redefined as described produces a complex output. The derivative of the real function $f(x)$ can be computed by expanding the complex operator $f(x+ih)$ as:

$$f(x+ih) = f(x) + ihf'(x) + \cdots \tag{38}$$

from which the derivative $f'(x)$ can be easily determined as:

$$f'(x) = \frac{Im[f(x+ih)]}{h} \tag{39}$$

As in the case of finite-differencing, the complex step-based differentiation also requires a step size. However, unlike finite-differencing the complex step method is insensitive to small step sizes since no differencing is required. In theory it is possible to verify forward and adjoint-based gradients using the complex step method to machine precision. With this in mind, a complex version of the complete coupled aero-structural analysis code has been constructed through scripting of the original source code to redefine variables from real to complex types and to overload a small number of functions for use with complex variables.

VIII. RESULTS

VIII.A. Time Dependent Analysis Problem

The chosen test case is a four bladed HART2 rotor in a forward flight condition. The flight condition parameters are: Mach numbers, $M_{tip} = 0.638, M_\infty = 0.095$, shaft tilt angle towards freestream, $\alpha_{shaft} = 5.4^\circ$. The corresponding rotor rotational speed is $\Omega = 1041$ RPM. The pitch angle actuation is prescribed as: $\theta = \theta_0 + \theta_{1s}sin(\psi) + \theta_{1c}cos(\psi)$, with $\theta_0 = 5.0^\circ, \theta_{1s} = -1.1^\circ, \theta_{1c} = 2.0^\circ$. The rotor is impulsively started from rest, in an initially quiescent flow field, and rotated with the mesh as a solid body for a fixed number of revolutions. This problem is solved both for a rigid blade model (using no structural model), as well as for a flexible blade model (using the beam structural model). For the latter, the flow is solved in tight coupling mode with the beam solver.

The baseline simulation (coarse mesh) makes use of a mixed element mesh made up of prisms, pyramids and tetrahedra consisting of approximately 2.32 million grid points and is shown in Figure (2(a)). The simulations are run for 5 rotor revolutions using a 2 degree time-step, i.e. for 900 time-steps starting from freestream initialization. For the rigid blade simulation, the time-dependent mesh motion is determined by first pitching the blade about the blade axis followed by solving the mesh deformation equations and then rotating the entire mesh as a solid body at each time step. The unsteady Reynolds-averaged Navier-Stokes equations are solved at each time step in ALE form, using the Spalart-Allmaras turbulence model.

The coupled CFD/CSD simulation is run in a similar manner. However, the flow solution (CFD) is coupled with the beam solver (CSD) at every time step by appropriately exchanging, a) airloads information from the flow domain to the beam and b) blade deformation information from the beam to the flow domain, at the fluid-structure interface (i.e. blade surface). In this coupled simulation, the mesh is moved according to the deformations dictated by the new flexed blade coordinates determined from the structural beam code after the combined kinematics of pitch actuation followed by solid body rotation of the entire mesh have been performed. Thus, the flow now sees not only the pitched and rigidly rotated mesh (observed in rigid blade simulation in forward flight), but also the deformed mesh around the blades due to both pitching and structural deformations. This coupled fluid-structure interaction problem needs to be iterated until satisfactory convergence is achieved on flow, structure and mesh deformation problems within each time step. This kind of CFD/CSD coupling done within every time step is known as *tight coupling*.

The simulations were performed on the Yellowstone supercomputer at the NCAR-Wyoming Supercomputing Center (NWSC), with the analysis problem running in parallel on 1024 cores. Each time step used 6 coupling iterations, and each coupling iteration used 10 non-linear flow iterations with each non-linear iteration consisting of a three-level line-implicit multigrid cycle. The typical simulation at this level of resolution requires approximately 40 minutes of wall clock time per rotor revolution. Figure (2(b)) shows the Q-criterion isosurfaces for the flexible rotor after 5 revolutions. The figure clearly shows how the wakes from both the root and tip of upstream blades interact with the trailing blades resulting in complex flow features, although these are diffused due to the coarse mesh resolution.

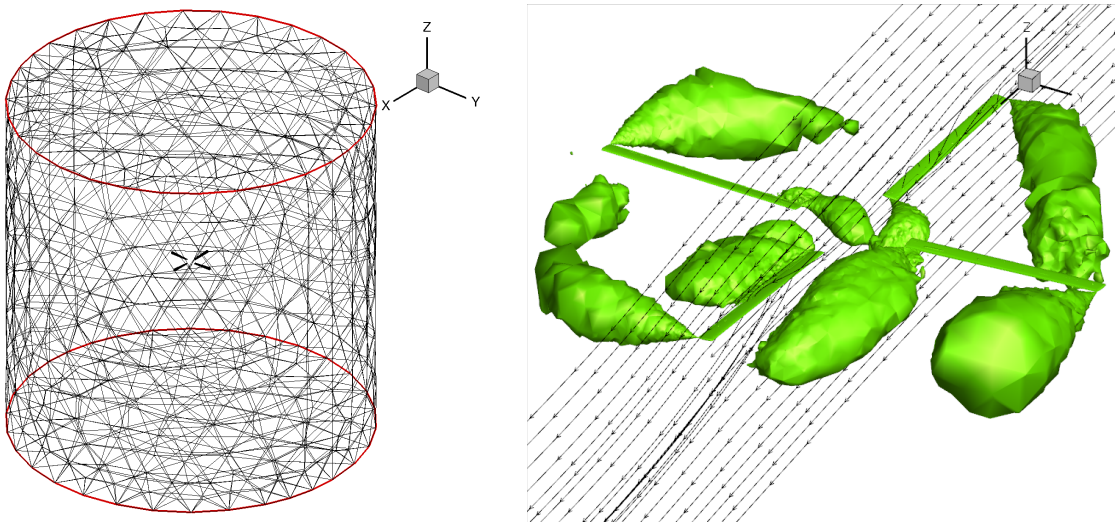

(a) Computational Domain: 2.32 million nodes (b) Q-criterion

Figure 2. Computational polyhedra mesh and Q-criterion for the flexible baseline HART2 rotor in forward flight after 5 revolutions

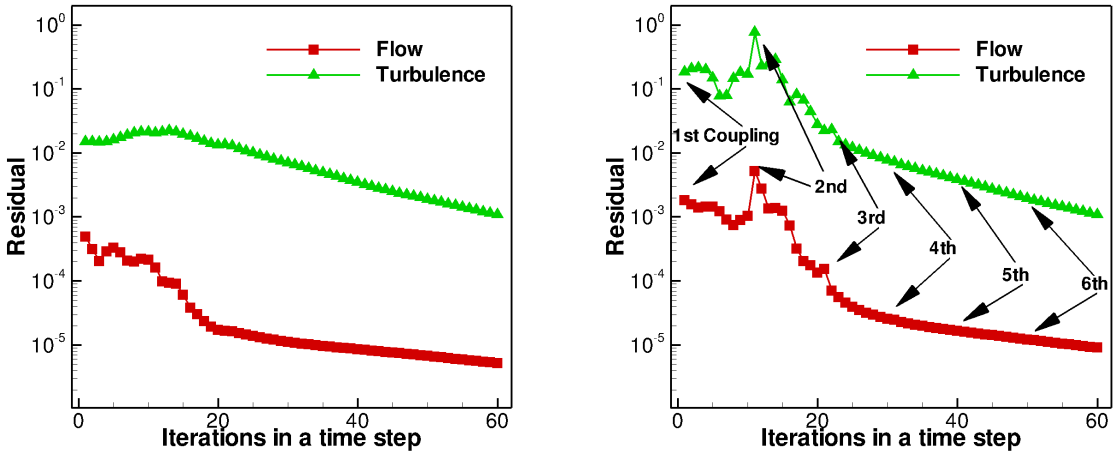

(a) Rigid Blade (b) Flexible Blade

Figure 3. Flow and turbulence residual convergence at a given time step for rigid and flexible blade analysis

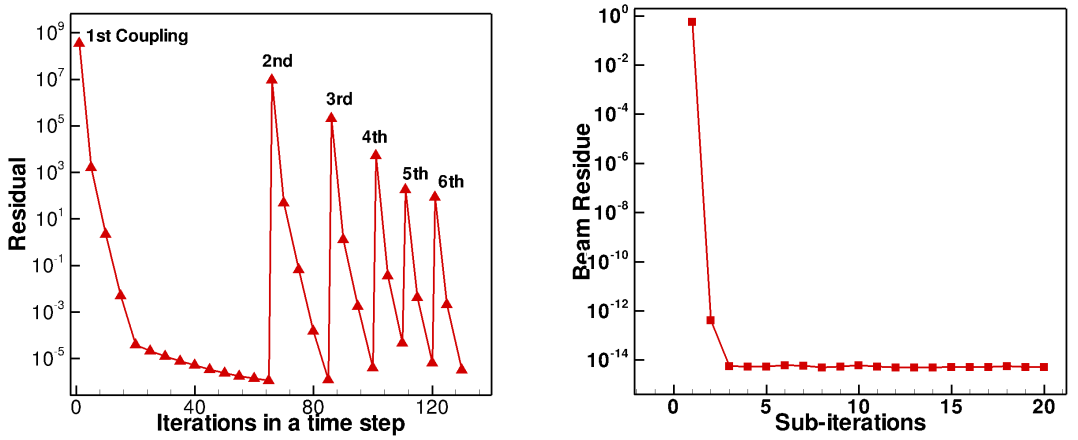

(a) Mesh Convergence per time step for coupled analysis

(b) Beam and FSI convergence per coupling iteration

Figure 4. Residual convergence of mesh and beam (overall FSI) in one coupling iteration

Figures 3 and 4 summarize the overall convergence of the rigid and aero-elastic coupling analysis formulations. Figure 3(a) shows the typical flow and turbulence residual convergence within a single time step for the rigid rotor case (no structural model), while Figure 3(b) depicts convergence of the flow and turbulence residuals at the same time step for the coupled aeroelastic case. In this case, the jumps in residual values at the start of new coupling iterations are clearly visible, although these jumps become smaller as the coupling procedure converges. The overall residual histories closely follow those of the rigid rotor case after the first few coupling iterations. Figure 4(a) depicts the convergence of the mesh deformation residual for the same time step, also showing jumps in the residual at the start of each new coupling iteration. Solution of the mesh deformation equations terminates when the residuals reach a prescribed tolerance of $1.e-06$, and hence the variable number of iterations per coupling cycle. Most notable is the fact that the initial mesh deformation residual decreases at each new coupling iteration, providing a measure of the convergence of the entire coupling procedure. The corresponding beam residual drop is observed to be of 15 orders of magnitude, as shown in Fig. 4(b). Figure 4(b) illustrates the convergence of the coupled beam/FSI residual (i.e. equations (26) and (27)), showing rapid convergence to machine zero in a small number of iterations within a single CFD/CSD coupling iteration.

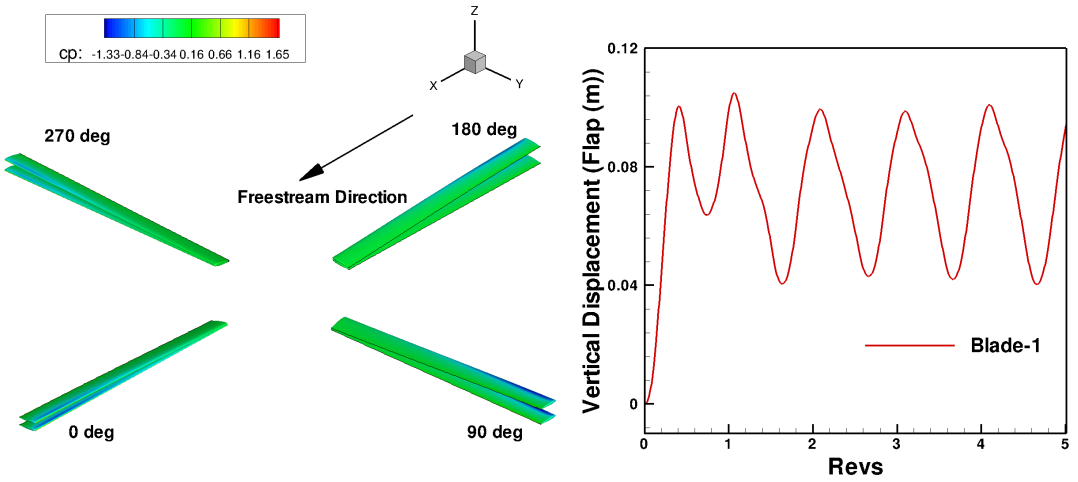

(a) Blade Deformation (C_p contours)

(b) Blade-1 tip vs time

Figure 5. HART2 blade deformation

The effect of the CFD/CSD aeroelastic coupling is clearly demonstrated in Figure 5(a), which compares the deformed blade shape and its corresponding C_p surface contours from the coupled simulation with that from the rigid blade simulation. From the figure it is noted that all four blades show different deformation characteristics due to corresponding different aerodynamic environment they experience in a forward flight. The blade attains the largest flap displacement at azimuth, $\psi = 180^\circ$ and the smallest flap displacement at azimuth, $\psi = 0^\circ$. For both the flexible and rigid blades, the pressure contours demonstrate that the advancing side blades experience more compressibility effects (larger pressure gradients near the rotor tips) than the retreating side blades. The flexible blade tip vertical displacement time history shown in Figure 5(b) demonstrates $1/rev$ behavior of blade flapping.

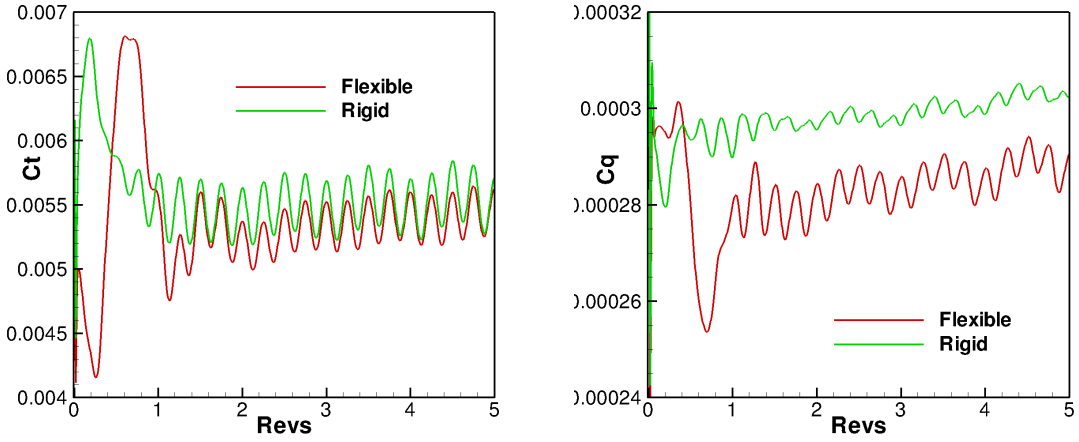

(a) C_T vs time (b) C_Q vs time

Figure 6. Performance comparison of flexible blade with rigid blade

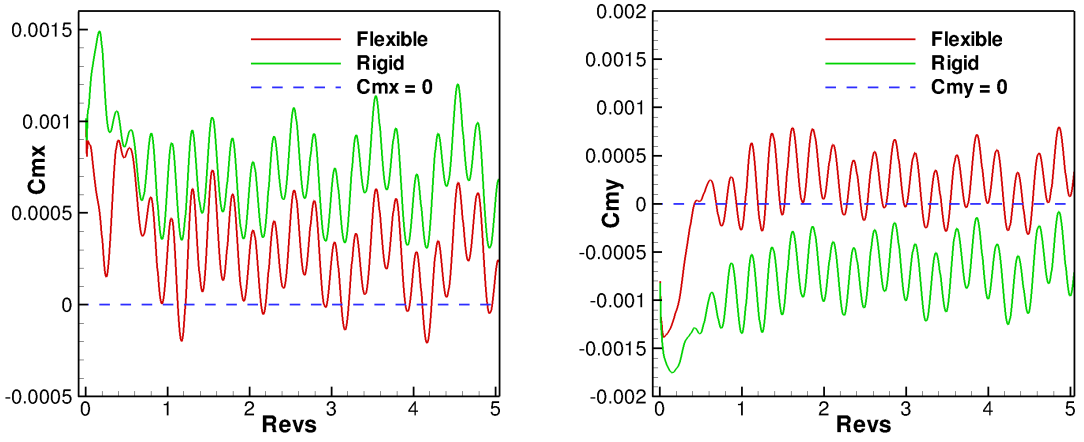

(a) Lateral moment vs time (b) Longitudinal moment vs time

Figure 7. Rotor moments comparison of flexible blade with rigid blade

Figures (6) summarizes performance comparison between flexible and rigid blades over 5 rotor revolutions. Besides showing consistent 4/rev harmonic content in the airloads, the figures also show that the rigid blades over predict thrust and power compared to flexible blades. This suggests that performance predictions might be erroneous if the aeroelastic nature of rotor blade is not taken into account. Figures (7) further compare the rotor longitudinal (C_{M_Y}) and lateral (C_{M_X}) moments of the flexible rotor with the rigid one. It should be noted that neither the rigid nor the flexible rotor are in a moment trimmed state (zero mean moment) at the prescribed pitch parameters.

VIII.B. Fully Coupled Unsteady Aeroelastic Adjoint Sensitivity Verification

VIII.B.1. Geometry Parameterization

In order to obtain sensitivities with respect to a set of shape parameters that are well suited for design optimization purposes, a baseline blade is constructed by stacking 11 airfoil section along the span. Each airfoil contains 10 Hicks-Henne bump functions, 5 on the upper surface, and 5 on the lower surface, that can be used to modify the airfoil shape. Additionally, the twist values of the blade at the root and tip airfoil sections are also used as design variables resulting in a total of 112 design variables. Figure (8(a)) provides an illustration of the baseline blade design setup. A high density structured mesh is generated about this blade geometry, which is then rotated and translated to match each individual blade in the CFD mesh, as shown in Figure (8(b)). Interpolation patterns between each unstructured mesh surface point and the baseline structured mesh are determined in a preprocessing phase. These interpolation patterns are then used to interpolate shape changes from the baseline blade to all four blades in the CFD mesh (as determined by changes in the design variables) and to transfer sensitivities from the surface CFD mesh points to the design variables using the chain rule of differentiation.

In addition to the aforementioned design variables, inclusion of control parameters for pitching in forward flight introduces a new set of (at least three) design parameters, i.e. $\mathbf{D} = [\theta_{\mathbf{0}}, \theta_{\mathbf{c_i}}, \theta_{\mathbf{s_i}}]$. Design variable $\theta_{\mathbf{0}}$ is known as rotor collective pitch angle and $\theta_{\mathbf{c_i}}$ and $\theta_{\mathbf{s_i}}$ are rotor cyclic pitch angles. This results in a total of 115 design variables. Thus the blade transformation matrix (denoted by $[\mathbf{T}^{\theta}(\theta)]$ in VI.A) is now linearized with respect to these additional design variables. These sensitivities, in addition to the above mentioned geometric sensitivities, are transfered onto the CFD interior mesh points from the CFD surface mesh points through the interpolation method described earlier.

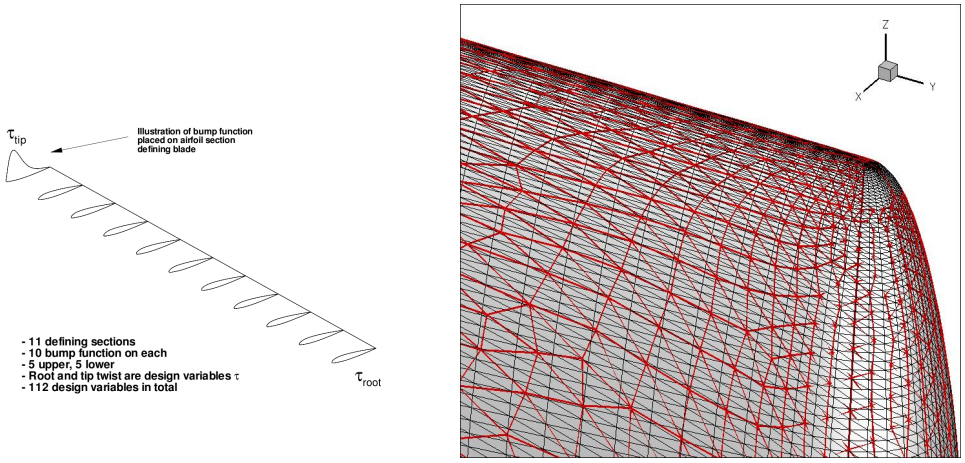

(a) Blade design parameters (b) Baseline structured blade mesh overlap with CFD mesh

Figure 8. Illustration of (a) baseline blade with design parameters and (b) overlap in tip region between baseline blade structured mesh and CFD surface unstructured mesh.

VIII.B.2. Unsteady Objective Function Formulation

A time-integrated objective function based on the time variation of the thrust (C_T), torque (C_Q) and moment coefficients (C_{M_X} and C_{M_Y}) are used for this test case. The goal of the optimization is to reduce the time-integrated torque coefficient while constraining the time-integrated thrust coefficient to the baseline rotor performance as well as constraining the moment coefficients along roll (C_{M_X}) and pitch (C_{M_Y}) axes of the rotor to a trimmed value, i.e. zero moment values. The objective function is based on the summation of the differences between a target and a computed

objective value at each time level n . Mathematically the global objective function is defined as:

$$
\begin{aligned}
L^g &= L_{Shape} + L_{Trim} && (40)\\
L_{Shape} &= \omega_1 \frac{1}{T} \sum_{n=1}^{n=N} \Delta t \left[\delta C_Q^n\right]^2 && (41)\\
L_{Trim} &= \omega_2 \frac{1}{T} \sum_{n=1}^{n=N} \Delta t \left[\delta C_T^n\right]^2 + \omega_3 \left[\delta \bar{C}_{M_X}\right]^2 + \omega_4 \left[\delta \bar{C}_{M_Y}\right]^2 && (42)\\
\delta C_Q^n &= (C_Q^n - C_{Q target}^n) && (43)\\
\delta C_T^n &= (C_T^n - \bar{C}_{T target}) && (44)\\
\delta \bar{C}_{M_X} &= \frac{1}{T} \sum_{n=1}^{n=N} \Delta t (C_{M_X}^n - C_{M_X target}^n) && (45)\\
\delta \bar{C}_{M_Y} &= \frac{1}{T} \sum_{n=1}^{n=N} \Delta t (C_{M_Y}^n - C_{M_Y target}^n) && (46)
\end{aligned}
$$

where the mean target thrust coefficient value is specified to the Hart2 baseline mean trim value of $\bar{C}_{T target} = 4.4e-3$, and the target torque and moment values are set to zero. The weights $(\omega_i, i = [1,2,3,4])$ are included to equalize the difference in orders-of-magnitude between the thrust, torque and moment coefficients. Use of pitch control parameters $([\theta_0, \theta_{c_i}, \theta_{s_i}])$ as design variables and use of moment penalty terms ensure that the optimized rotor shape with optimized control parameters tend towards a final trimmed state when the rotor design cycles converge. This approach is computationally more efficient than the use of a hard constraint formulation, since this latter approach would require the computation of multiple adjoint problems at each design cycle, as opposed to the single adjoint required in the current formulation. However, the trim constraint may not be satisfied exactly in this approach.

VIII.B.3. Unsteady Adjoint Sensitivity Verification

The fully coupled CFD/CSD adjoint formulation was verified by comparing its sensitivities with those obtained from the tangent as well as the complex step method. The coupled adjoint formulation was verified for perturbations on one geometric design parameter, namely, collective pitch (θ_0), for both uncoupled (rigid blade) as well as coupled (flexible blade) simulations. A complex perturbation of size 1×10^{-100} is introduced on collective pitch at the beginning of the analysis run. The design sensitivities of the functional ($\frac{\partial L^g}{\partial D}$) obtained from complex, tangent and adjoint formulations are compared after every time instance for up to 5 time steps – see Table (1). Both the rigid and the fully coupled aeroelastic problems are converged to machine zero at each time step in order to avoid contaminating the sensitivity values with errors due to incomplete convergence. The rigid sensitivity verification serves as a sanity check of the new forward sensitivity formulation for forward flight conditions when the structural code is switched off. As can be seen from the table, the sensitivities agree to at least 13 significant digits for both the rigid and flexible aeroelastic rotor cases.

IX. Performance Optimization of Helicopter Rotor in Forward Flight

The optimization tool thus verified is applied to the flexible HART2 rotor using the same time-dependent test case as described in the analysis section. The simulation is run for two full rotor revolutions, starting impulsively from rest in quiescent flow. The objective consists of the time-integrated torque with thrust and moment penalty, as described previously. However, the objective to be minimized is only integrated over the last one revolution, in order to avoid the optimization process from focusing on start-up transients. The optimization problem is solved on a relatively coarse grid (2.3 million points) using a time step size of 2.0 degrees. Figures 9 shows the residual convergence for a typical unsteady adjoint time step for $\Delta t = 2^\circ$. The figure shows the residual drops by 5 orders of magnitude over 6 coupling cycles.

The optimization procedure used is the L-BFGS-B bounded reduced Hessian algorithm.[30] Each request by the optimization driver for a function and gradient value results in a single forward time-integration of the analysis solver and a single backward integration in time of the adjoint solver. A bound of $\pm 5\%$ chord for each defining airfoil section was set on the Hicks-Henne bump functions, a bound of $\pm 1.0^\circ$ of twist was set on the root and tip twist

Table 1. Adjoint sensitivity verification for Forward Flight

n	Method	Uncoupled (Rigid)	Coupled (Aero-elastic)
1	Complex	8.135662924562**930**E-005	7.569817143673**123**E-005
	Tangent	8.135662924562**923**E-005	7.569817143673**061**E-005
	Adjoint	8.135662924562**884**E-005	7.569817143672**761**E-005
2	Complex	7.303561433847**516**E-005	6.040142774935**852**E-005
	Tangent	7.303561433847**498**E-005	6.040142774935**835**E-005
	Adjoint	7.303561433847**042**E-005	6.040142774935**570**E-005
3	Complex	1.579075715783**277**E-005	-4.959909870786**381**E-006
	Tangent	1.579075715783**178**E-005	-4.959909870787**765**E-006
	Adjoint	1.579075715780**985**E-005	-4.959909870785**228**E-006
4	Complex	-3.279789405316**752**E-005	-6.193896187819**846**E-005
	Tangent	-3.279789405316**760**E-005	-6.193896187820**087**E-005
	Adjoint	-3.279789405324**491**E-005	-6.193896187820**419**E-005
5	Complex	-7.466264294860**007**E-005	-1.142069116982**308**E-004
	Tangent	-7.466264294859**811**E-005	-1.142069116982**308**E-004
	Adjoint	-7.466264294878**836**E-005	-1.142069116982**432**E-004

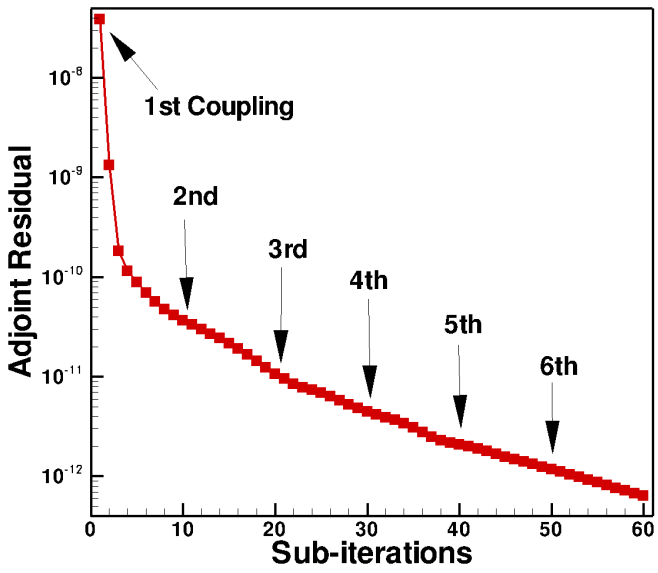

Figure 9. Residual convergence in a typical adjoint time step

definitions, and a bound of $\pm 5.0^{\circ}$ of pitch angle was set on all the pitch parameters (collective and cyclics). The optimizations were performed on the Yellowstone supercomputer at the NCAR-Wyoming Supercomputing Center (NWSC) with the simulations (analysis/adjoint) running in parallel on 1024 cores. Each time step in the analysis problem employed 6 coupling cycles. Each coupling cycle used 10 nonlinear iterations. A typical coupled functional gradient (analysis/adjoint) computation step requires approximately 70 minutes when run on 1024 cores.

The performance optimization consists of three main stages: i) Trim ii) Shape/performance optimization and, iii) re-trim. The 'Trim' step involves trimming the rotor to a target wind tunnel rotor thrust value of $C_T = 4.4e-3$ and zero longitudinal and lateral moments ($C_{M_Y}, C_{M_X} = 0$). The objective function used in this step consists only of the thrust and moment terms in Eqn 40 ($\omega_1 = 0$) and the objective minimization is performed using only the three pitch parameters, namely, collective and cyclics as design variables.

In the second stage, blade shape optimization is performed by including the performance objective, i.e., C_Q term into the time dependent objective function to be minimized. Appropriate weights ($\omega_i, i = 1,2,3,4$) are used to maintain the rotor trim state through a penalty function while the blade shape is optimized to obtain minimum rotor power. In total 115 design parameters were used in this stage, including 112 blade shape parameters and 3 pitch control parameters. However, even after optimization convergence in stage two, the exact trim state is not maintained. This is because the trim objective components in the objective function were used only as weak constraint terms, i.e. as penalty terms and not as hard constraints. Therefore, the last stage involves trimming the rotor back to the target thrust and moment values, once again using only the three control pitch parameters as design inputs. This stage is otherwise referred to as the 're-trim' stage in this paper.

The optimization results for the rigid blade case are presented first, followed by the flexible blade optimization results. Figure 10 demonstrates that the rigid HART2 rotor was successfully trimmed to the target rotor thrust ($C_T = 4.4e-3$) and moment values ($C_{M_X}, C_{M_Y} = 0$). Fig. 11(a) shows that the trim objective gradient drops by more than 5 orders of magnitude, while the objective functional achieves a minimum over 26 design iterations. Figure 11(b) further shows consistent convergence of all the three pitch parameters.

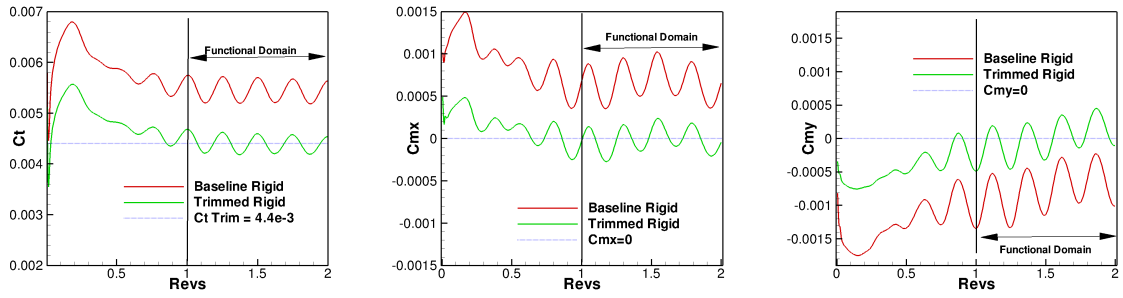

(a) Thrust trim (b) Lateral moment trim (c) Longitudinal moment trim

Figure 10. HART2 rigid blade trim

Figures 12 summarizes the optimized rotor blade shape as well as re-trimmed rotor performance plots. Figure. 12(a) shows that the baseline trimmed rigid rotor is shape optimized to achieve approximately 4.7% power reduction with a penalty of approximately 2.3% thrust loss. Although some of this gain is lost upon retrim, the final optimized and trimmed rotor achieves an overall 2.8% reduction in power compared to the baseline blade. The near identical lines of the baseline and retrimmed rotor thrust plots in Figure. 12(b) confirms that the rotor is retrimmed back to the trim target thrust value. Figure. 12(c) shows 2 orders of magnitude gradient drop and consistent functional convergence after 35 design iterations for the blade shape optimization. Figure. 13 shows the shape optimized blade sections at 9 stations. The optimized blade shape results in thicker inboard and thinner outboard stations.

Figures 14 illustrates the trim optimization of the flexible HART2 rotor to the trim target thrust ($C_T = 4.4e-3$) and moment values ($C_{M_X}, C_{M_Y} = 0$). Fig. 15(a) shows that the trim objective gradient drops by more than 2 orders of magnitude, while the objective functional achieves a minimum over 19 design iterations. Figure 15(b) further shows consistent convergence of all the three pitch parameters.

Figures 16 summarizes the optimized flexible blade shape as well as re-trimmed performance plots. Figure. 16(a) shows the baseline trimmed flexible rotor is shape optimized to achieve a significant power reduction of approximately 5.0% with a thrust loss of approximately 2.6%. Similar to the rigid blade re-trim, even for the flexible blade, some of this gain is lost upon re-trim. However, the final shape optimized and re-trimmed rotor achieves an overall 3.1% reduction in power compared to the baseline blade. Figure. 16(c) shows one and half orders of magnitude gradient

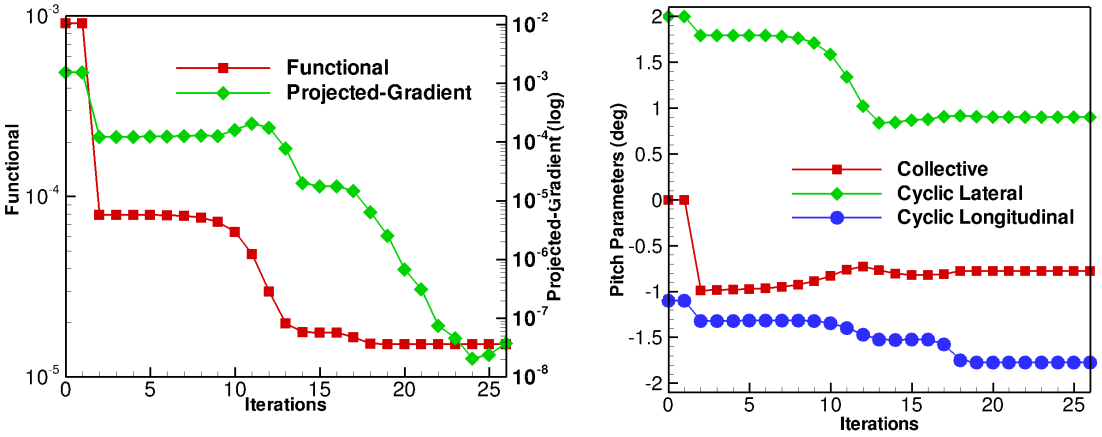

(a) Trim optimization convergence (b) Pitch parameters convergence

Figure 11. HART2 rigid blade trim convergence

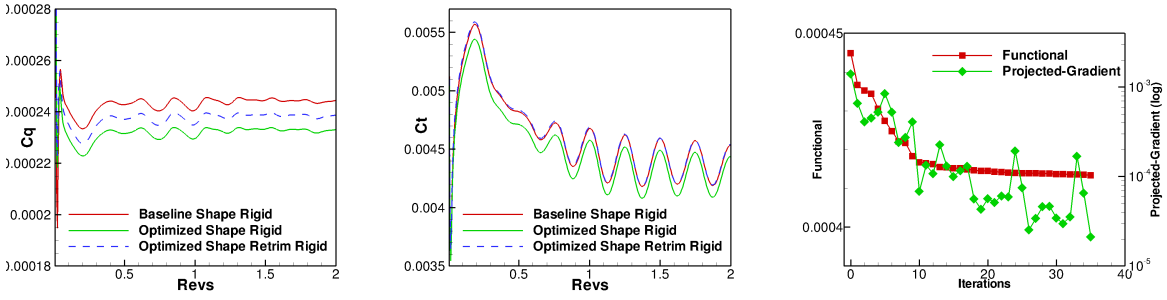

(a) Power time history (b) Thrust time history (c) Shape optimization convergence

Figure 12. HART2 rigid blade shape optimization and re-trim

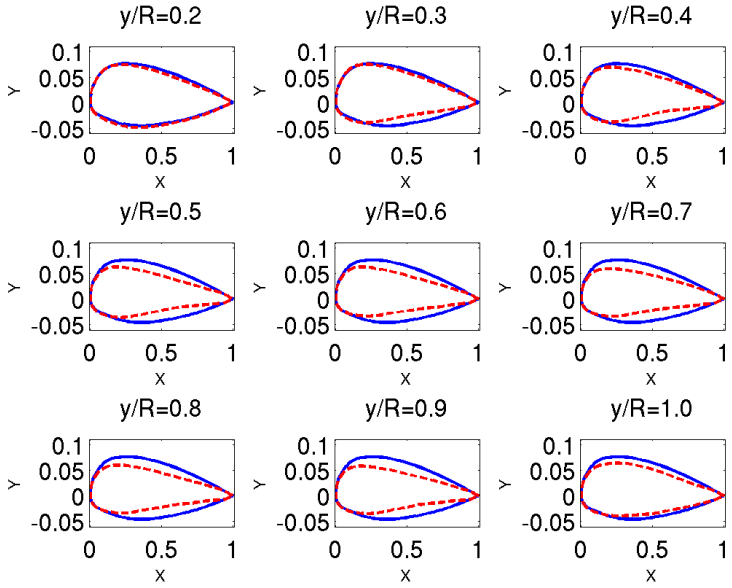

Figure 13. HART2 rigid blade optimized blade sections; solid-baseline, dashed-optimized

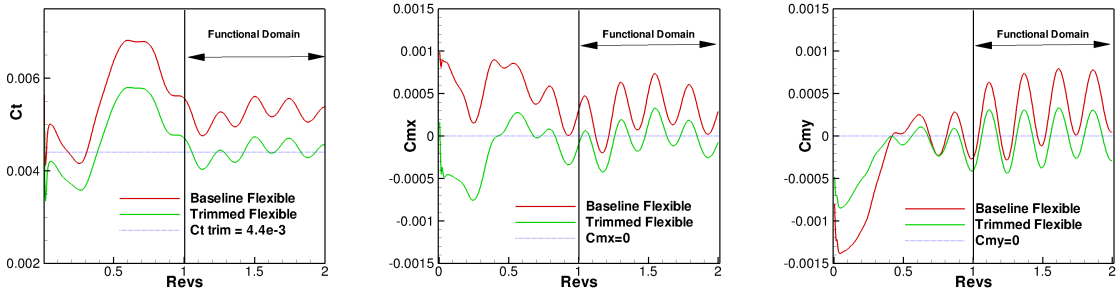

(a) Thrust trim (b) Lateral moment trim (c) Longitudinal moment trim

Figure 14. HART2 flexible blade trim

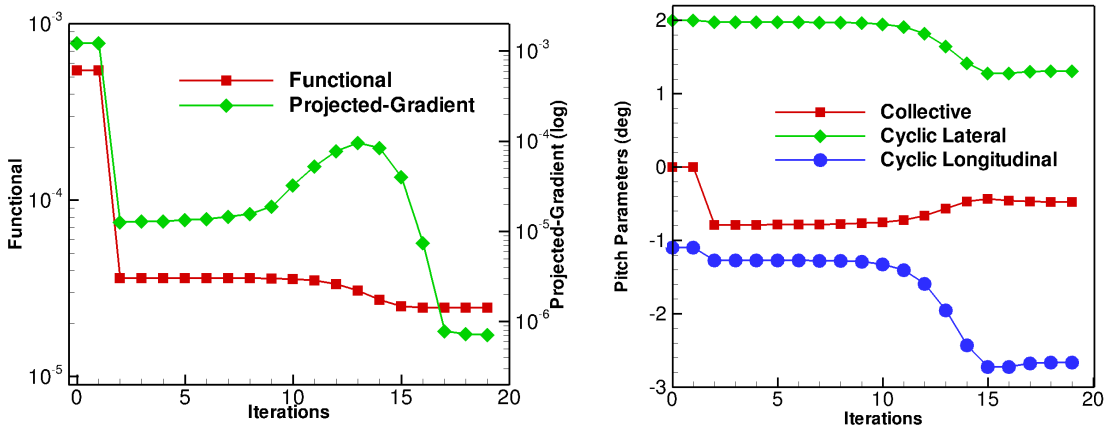

(a) Trim optimization convergence

(b) Pitch parameters convergence

Figure 15. HART2 flexible blade trim convergence

drop and consistent functional convergence even after 21 design iterations for the blade shape optimization stage. Figure. 17 shows the shape optimized blade sections at 9 stations. The optimized blade shapes show similar trend to those observed in the rigid blade shape optimization, i.e. thicker inboard and thinner outboard stations.

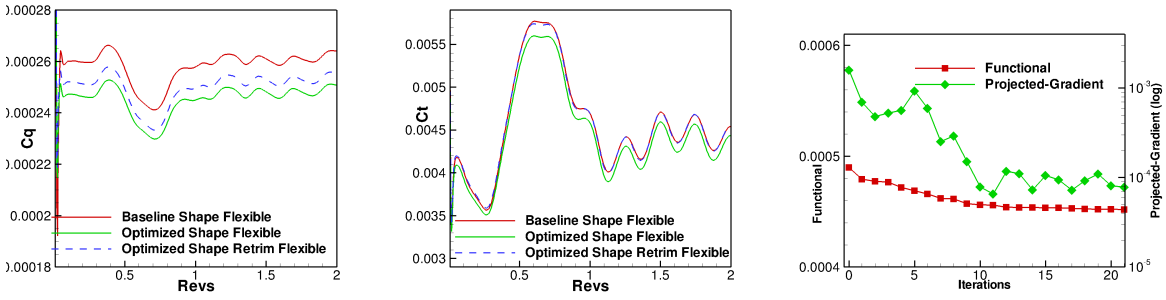

(a) Power time history

(b) Thrust time history

(c) Shape optimization convergence

Figure 16. HART2 flexible blade shape optimization and re-trim

X. Conclusions and Future Works

In this work, a discrete adjoint formulation for time-dependent tightly coupled aeroelastic three-dimensional problems of flexible rotors in forward flight conditions has been developed. The unsteady adjoint sensitivities of the formulation over several time steps have been verified. The current formulation for rotor problems in forward flight conditions was built upon a previously developed adjoint formulation for rotor problems in hover conditions, by incorporating a blade cyclic pitch capability in the analysis formulation as well as in tangent and adjoint sensitivity analysis formulations. The formulation is designed to reuse as much as possible the original coupled aeroelastic data-structures and solution strategies used for the analysis problem, thus simplifying implementation and verification.

After successful verification of the developed adjoint optimization tool, it was effectively used to perform efficient rotor blade shape design targeting minimum rotor torque with the constraint of a prescribed rotor trim state. The performance optimization on both rigid as well as flexible blades consistently resulted in approximately 3.0% power reduction over the baseline blade shape while sustaining a target trim state.

In the future, this work will be extended to carry out multipoint rotor design optimization, for example, for multiple flight conditions such as hover as well as forward flight. In addition, the future rotor design optimizations will include

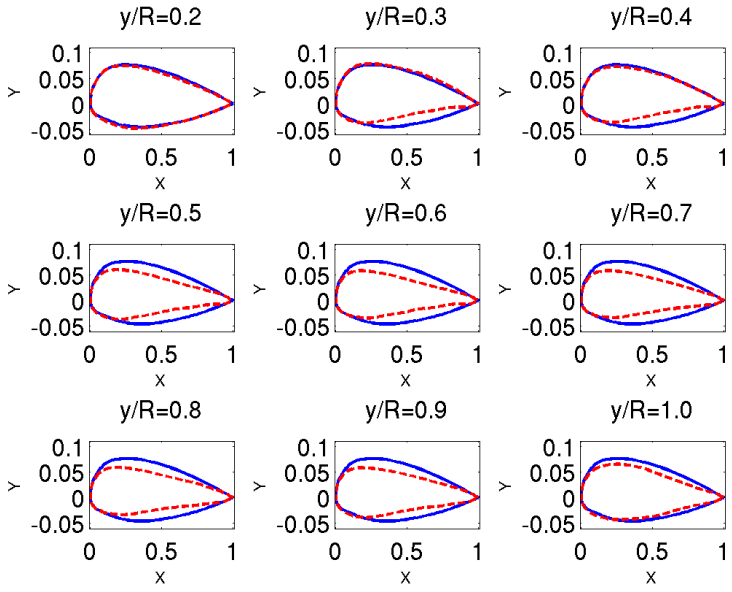

Figure 17. HART2 flexible blade optimized blade sections; solid-baseline, dashed-optimized

more blade geometric design parameters, such as, taper (or blade planform) and thickness, as well as the corresponding structural design parameters to accommodate these geometric changes, such as, mass and stiffness.

XI. Acknowledgements

This work was partly funded by the Alfred Gessow Rotorcraft Center of Excellence through a subcontract with the University of Maryland. Computer resources were provided by the University of Wyoming Advanced Research Computing Center and by the NCAR-Wyoming Supercomputer Center.

References

[1]Jameson, A., "Aerodynamic Shape Optimization using the Adjoint Method," *VKI Lecture Series on Aerodynamic Drag Prediction and Reduction, von Karman Institute of Fluid Dynamics, Rhode St Genese, Belgium*, 2003.

[2]Jameson, A. and Vassberg, J., "Computational Fluid Dynamics for Aerodynamic Design: Its Current and Future Impact," *Proceedings of the 39th Aerospace Sciences Meeting and Exhibit, Reno NV*, 2001, AIAA Paper 2001–0538.

[3]Nielsen, E. and Anderson, W., "Recent Improvements in Aerodynamic Design Optimization on Unstructured Meshes," *AIAA Journal*, Vol. 40, No. 6, June 2002, pp. 1155–1163.

[4]Jameson, A. and Martinelli, L., "Aerodynamic shape optimization techniques based on control theory," *Computational Mathematics Driven by Industrial Problems*, edited by R. Burkard, A. Jameson, G. Strang, P. Deuflhard, J.-L. Lions, V. Capasso, J. Periaux, and H. Engl, Vol. 1739 of *Lecture Notes in Mathematics*, Springer Berlin Heidelberg, 2000, pp. 151–221.

[5]Kim, S., J., A., and Jameson, A., "Multi-Element High-Lift Configuration Design Optimization Using Viscous Continuous Adjoint Method," *Journal of Aircraft*, Vol. 41, No. 5, 2004, pp. 1082–1097.

[6]K., N. S., Jameson, A., and Alonso, J., "Adjoint-Based Sonic Boom Reduction for Wing-Body Configurations in Supersonic Flow," *Canadian Aeronautics and Space Journal*, Vol. 51, No. 4, 2005.

[7]Jameson, A. and K., N. S., "Optimum Shape Design for Unsteady Flows with Time-Accurate Continuous and Discrete Adjoint Method," *AIAA Journal*, Vol. 45, No. 7, 2007, pp. 1478–1491.

[8]Palaniappan, K., Sahu, P., Jameson, A., and Alonso, J. J., "Design of Adjoint-Based Laws for Wing Flutter Control," *Journal of Aircraft*, Vol. 48, No. 1, 2011, pp. 331–335.

[9]Giles, M., Duta, M., Muller, J., and Pierce, N. A., "Algorithm Developments for Discrete Adjoint Methods," *AIAA Journal*, Vol. 41, No. 2, February 2003, pp. 198–205.

[10]Mavriplis, D. J., "Solution of the Unsteady Discrete Adjoint for Three-Dimensional Problems on Dynamically Deforming Unstructured Meshes," *Proceedings of the 46th Aerospace Sciences Meeting and Exhibit, Reno NV*, 2008, AIAA Paper 2008–0727.

[11]Nielsen, E. and Diskin, B., "Discrete Adjoint-Based Design for Unsteady Turbulent Flows on Dynamic Overset Unstructured Grids," *50th AIAA Aerospace Sciences Meeting and Exhibit, Nashville, TN*, January 9-12 2012, AIAA Paper 2012–0554.

[12]Nielsen, E. J., Diskin, B., and Yamaleev, N., "Discrete Adjoint-Based Design Optimization of Unsteady Turbulent Flows on Dynamic Unstructured Grids," *AIAA Journal*, Vol. 48-6, June 2010, pp. 1195–1206.

[13]Nielsen, E. J., Lee-Rausch, E. M., and Jones, W. T., "Adjoint-Based Design of Rotors in a Noninertial Reference Frame," *Journal of Aircraft*, Vol. 47-2, March-April 2010, pp. 638–646.

[14]Mani, K. and Mavriplis, D. J., "Geometry Optimization in Three-Dimensional Unsteady Flow Problems using the Discrete Adjoint," *51st AIAA Aerospace Sciences Meeting, Grapevine, TX*, January 2013, AIAA Paper 2013-0662.

[15]Martins, J. R. R. A. and Lambe, A. B., "Multidisciplinary Design Optimization: A Survey of Architectures," *AIAA Journal*, Vol. 51, 2013, pp. 2049–2075.

[16]Kenway, G. K. W., Kennedy, G. J., and Martins, J. R. R. A., "Scalable parallel approach for high-fidelity steady-state aeroelastic analysis and adjoint derivative computations," *AIAA Journal*, 2013, (In press).

[17]Mishra, A., Mani, K., Mavriplis, D. J., and Sitaraman, J., "Time-dependent Adjoint-based Optimization for Coupled Aeroelastic Problems," *21st AIAA CFD Conference, San Diego, CA*, June 24–27 2013, AIAA Paper 2013–2906.

[18]Mishra, A., Mani, K., Mavriplis, D. J., and Sitaraman, J., "Time-dependent Adjoint-based Aerodynamic Shape Optimization Applied to Helicopter Rotors," *70th American Helicopter Society Annual Forum, Montreal, QC, CA*, May 20–22 2014.

[19]Mavriplis, D. J., "Discrete Adjoint-Based Approach for Optimization Problems on Three-Dimensional Unstructured Meshes," *AIAA Journal*, Vol. 45-4, April 2007, pp. 741–750.

[20]Mavriplis, D. J., "Solution of the Unsteady Discrete Adjoint for Three-Dimensional Problems on Dynamically Deforming Unstructured Meshes," *Proceedings of the 46th AIAA Aerospace Sciences Meeting, Reno, NV*, 2008, AIAA Paper 2008–0727.

[21]Spalart, P. R. and Allmaras, S. R., "A One-equation Turbulence Model for Aerodynamic Flows," *La Recherche Aérospatiale*, Vol. 1, 1994, pp. 5–21.

[22]Mavriplis, D. J., "Multigrid Strategies for Viscous Flow Solvers on Anisotropic Unstructured Meshes," *Journal of Computational Physics*, Vol. 145, No. 1, Sept. 1998, pp. 141–165.

[23]Yang, Z. and Mavriplis, D. J., "A Mesh Deformation Strategy Optimized by the Adjoint Method on Unstructured Meshes," *AIAA Journal*, Vol. 45, No. 12, 2007, pp. 2885–2896.

[24]Mavriplis, D. J., Yang, Z., and Long, M., "Results using NSU3D for the first Aeroelastic Prediction Workshop," *Proceedings of the 51st Aerospace Sciences Meeting and Exhibit, Grapevine TX*, 2013, AIAA Paper 2013–0786.

[25]Mani, K. and Mavriplis, D. J., "Adjoint based sensitivity formulation for fully coupled unsteady aeroelasticity problems," *AIAA Journal*, Vol. 47, No. 8, Aug. 2009, pp. 1902–1915.

[26]Schuster, D. M., Chwalowski, P., Heeg, J., and Wieseman, C. D., "Summary of Data and Findings from the First Aeroelastic Prediction Workshop," *Seventh International Conference on Computational Fluid Dynamics (ICCFD7)*, ICCFD, Big Island, HI, July 9-13 2012.

[27]Mishra, A., Mani, K., Mavriplis, D. J., and Sitaraman, J., "Helicopter Rotor Design using Adjoint-based Optimization in a Coupled CFD-CSD Framework," *69th American Helicopter Society Annual Forum, Phoenix, AZ*, May 21–23 2013.

[28]Yu, Y. H., Tung, C., van der Wall, B., Pausder, H.-J., Burley, C., Brooks, T., Beaumier, P., Delrieux, Y., Mercker, E., and Pengel, K., "The HART-II Test: Rotor Wakes and Aeroacoustics with Higher-Harmonic Pitch Control (HHC) Inputs -The Joint German/French/Dutch/US Project-," *58th American Helicopter Society Annual Forum, Montreal, Canada*, June 11–13 2002.

[29]Smith, M. J., Lim, J. W., van der Wall, B. G., Baeder, J. D., Bierdron, R. T., Boyd Jr., D. D., Jayaraman, B., Junk, S. N., and Min, B.-Y., "Adjoint-based Unsteady Airfoil Design Optimization with application to Dynamic Stall," *68th American Helicopter Society Annual Forum, Fort Worth, TX*, May 1–3 2012.

[30]Zhu, C., Byrd, R. H., Lu, P., and Nocedal, J., "L-BFGS-B - FORTRAN Subroutines for Large-scale Bound Constrained Optimization," Tech. rep., Department of Electrical Engineering and Computer Science, December 31 1994.